PERGAMON

International Journal of Solids and Structures 40 (2003) 6001–6022

INTERNATIONAL JOURNAL OF SOLIDS and STRUCTURES

www.elsevier.com/locate/ijsolstr

Craft—a plastic-damage-contact model for concrete. II. Model implementation with implicit return-mapping algorithm and consistent tangent matrix

A.D. Jefferson *

Division of Civil Engineering, P.O. Box 925, Cardiff University, CF24 0YF Cardiff, UK

Received 31 January 2003; received in revised form 16 June 2003

Abstract

A computational strategy for the evaluation of stresses in a finite element implementation of a new plastic-damage-contact model is described. As part of this strategy a new return-mapping algorithm is developed which fully couples plasticity to directional damage on one or more damage surfaces, and which ensures that local and total constitutive relationships are simultaneously satisfied. In addition, an associated consistent tangent matrix is derived. The performance of the model, as implemented with this new strategy, is explored in a range of 2D and 3D examples which include analyses based on direct and indirect fracture tests, a mixed mode fracture test, shear-normal tests in which aggregate interlock is significant and a reinforced concrete test in which cracking, aggregate interlock and crushing all contribute significantly to the behavior. It is concluded that the consistent computational approach gives solutions with good equilibrium convergence properties. Furthermore, it is concluded that the new model, as implemented in the finite element code, is able to represent a wide range of the behavior of plain and reinforced concrete structures.

Keywords: Constitutive; Damage; Fracture; Plasticity; Concrete; Integration; Return-mapping

1. Introduction

The type of stress return-mapping algorithm and the form of tangent constitutive matrix employed in the implementation of a constitutive model in a finite element program have an enormous impact upon the robustness and efficiency of the solution process and upon the accuracy of results obtained. For elasto-plastic models implicit algorithms for stress computations and associated consistent tangent matrices are nowadays largely preferred because, despite the increased computational effort, they result in better convergence and more accurate results than those of algorithms based upon explicit integration schemes (Simo and Hughes, 1998).

* Tel.: +44-29-2087-4263; fax: +44-29-2087-4597.
E-mail address: jeffersonad@cf.ac.uk (A.D. Jefferson).

0020-7683/$ - see front matter © 2003 Elsevier Ltd. All rights reserved.
doi:10.1016/S0020-7683(03)00391-3

The principles of the consistent approach were established by Simo and Taylor (1985), and have since been applied by many researchers to various plasticity models, e.g. Borja (1991), Larsson and Runesson (1996). Ortiz and Martin (1989) have studied the conditions for maintaining symmetry of the tangent constitutive operator and the implications for solutions in which such symmetry is not maintained. In some recent work, explicit expressions were derived for the consistent tangent matrix which avoided the inversion of a fourth order plastic flow rate gradient tensor (Palazzo et al., 2000; Le Van and de Saxcé, 2000), an operation which can be computationally expensive.

Implicit integration algorithms have also been presented for plastic damage models. de Souza Neto and Perić (1996) describe an implicit algorithm for an elasto-plastic isotropic damage model at finite strains, Johansson et al. (1999) present an algorithm for a viscoplastic model coupled to scalar damage, but with micro-crack-closure and reopening, and Armero and Oller (2000) describe an implicit method for a plastic damage model for porous metals, which also accounts for the opening and closing of voids. Recently, Lee and Fenves (2001) have presented an efficient returning mapping algorithm for a plastic damage model that employs a spectral decomposition of the stress matrix. The aforementioned algorithms were all for models that used scalar damage variables, but Mahnken et al. (2000) describe the implementation of Ortiz's (1985) model, which, for the mortar component, uses an anisotropic damage formulation that has a fourth order damage compliance tensor. For this model, the fully implicit approach developed requires the computation of the derivatives of the principal stress and projection tensors with respect to the Cartesian stress components. Whilst the model is quite different from the model referred to in this paper, a similar set of derivatives is required by the present algorithm, and therefore the work of Mahnken et al. (2000) is of particular relevance to the present work.

A model for concrete is described in an associated paper Jefferson (2003) which couples directional damage to plasticity and which employs contact mechanics to simulate crack opening–closing and shear contact effects. The model uses damage planes, the stresses on which are governed by a local constitutive relationship, but which also satisfy the static constraint, i.e. that the local stresses are the transformed components of the total stress tensor. A key aspect of the development of the model was the derivation of a so-called 'total–local' condition that ensures that both the local and total constitutive relationships are satisfied.

This paper describes the implementation of the Craft model and in particular a new implicit stress return-mapping algorithm for the plastic-damage-contact model. The paper also includes a number of finite element analysis examples that are used to study the convergence properties of the solutions, the ability of the model in a finite element context to simulate experimental behavior and also to judge the effects and accuracy of the new contact approach to the simulation of aggregate interlock.

The constitutive model has been implemented in the finite element program LUSAS (FEA Ltd, 2002), which was used for all of the simulations described later in the paper.

2. Model relationships

The model is described fully in the associated paper and therefore only the relationships essential for the description of the present algorithm will be presented here.

The stresses satisfy the yield condition

$$F(\boldsymbol{\sigma}, \kappa) \leqslant 0 \tag{1}$$

where κ is the plastic parameter.

The plastic flow relationship is given by

$$\dot{\boldsymbol{\varepsilon}}_{\mathrm{p}} = \dot{\lambda} \frac{\partial G}{\partial \boldsymbol{\sigma}} \tag{2}$$

where the superior dot denotes the time derivative, λ is the plastic multiplier and G the plastic potential function.

A modified work hardening function is used such that

$$\dot{\kappa} = X\boldsymbol{\sigma}^{\mathrm{T}}\frac{\partial G}{\partial \boldsymbol{\sigma}} \tag{3}$$

where X is a stress dependent parameter.

The local stress vector on a plane of degradation (POD) is related to the global stress tensor as follows

$$\mathbf{s}_i = \mathbf{N}_i\boldsymbol{\sigma} \tag{4}$$

where $\boldsymbol{\sigma}$ is the total stress tensor, $\mathbf{s}_i$ is the local stress vector which has one normal and two shear components with respect to the POD and $\mathbf{N}_i$ is the transformation matrix for POD i.

The relationship between the local effective strains ($\mathbf{e}$) and the local stresses is given by

$$\mathbf{s}_i = \mathbf{D}_{\mathrm{L}}\mathbf{M}_{x_i}\mathbf{e}_i = \mathbf{D}_{\mathrm{ls}_i}\mathbf{e}_i \tag{5}$$

in which $\mathbf{D}_{\mathrm{L}}$ is a local elastic constitutive matrix and $\mathbf{M}_x = \mathbf{M}_x\,(\mathbf{e}, \zeta, \kappa)$ is a local damage-contact matrix.

The 'fracture' component of the local strain is obtained as follows

$$\mathbf{e}_{\mathrm{f}_i} = (\mathbf{M}_{x_i}^{-1} - \mathbf{I})\mathbf{C}_{\mathrm{L}}\mathbf{s}_i = (\mathbf{I} - \mathbf{M}_{x_i})\mathbf{e}_i = \mathbf{C}_{\mathrm{lsf}_i}\mathbf{s}_i \tag{6}$$

The stress–'recoverable' strain relationship is given by

$$\boldsymbol{\sigma} = \left(\mathbf{I} + \mathbf{D}_{\mathrm{e}}\sum_{j=1}^{n_{\mathrm{p}}}\mathbf{N}_j^{\mathrm{T}}\mathbf{C}_{\mathrm{lsf}_j}\mathbf{N}_j\right)^{-1}\mathbf{D}_{\mathrm{e}}(\boldsymbol{\varepsilon} - \boldsymbol{\varepsilon}_{\mathrm{p}}) = \mathbf{D}_{\mathrm{efc}}(\boldsymbol{\varepsilon} - \boldsymbol{\varepsilon}_{\mathrm{p}}) \tag{7}$$

in which $\mathbf{I}$ is the identity matrix, n_{p} is the number of PODs, $\mathbf{D}_{\mathrm{e}}$ is the elastic constitutive matrix, ε_{p} is the plastic strain tensor.

3. Return-mapping algorithm

In the context of a finite element incremental–iterative solution for a time independent problem, the stress update is made from the previous converged state. The values of quantities on entry to and exit from the return-mapping algorithm are denoted by the subscripts k and $k+1$ respectively. The total change of any quantity from the last converged state is denoted by Δ and δ is used to denote the change of a quantity in a stress-update iteration.

In this section it will be assumed that the number of PODs and the need, or otherwise, to include plastic yield have already been established. The strategy used for making these choices and the way in which new PODs are formed are discussed in Section 5 of this paper.

The aim of the update algorithm is to compute the new stresses $\boldsymbol{\sigma}_{k+1}$ for the incremental strain $\Delta\boldsymbol{\varepsilon}$ from the previous stresses $\boldsymbol{\sigma}_k$ such that all of the following relationships are satisfied; the total constitutive relationship,

$$\boldsymbol{\sigma}_{k+1} = \mathbf{D}_{\mathrm{e}}\left(\boldsymbol{\varepsilon}_{k+1} - \boldsymbol{\varepsilon}_{\mathrm{p}_{k+1}} - \sum_{j=1}^{n_{\mathrm{p}}}\mathbf{N}_j^{\mathrm{T}}\mathbf{e}_{\mathrm{f}_{j_{k+1}}}\right) \tag{8}$$

the stress transformation;

$$\mathbf{s}_{k+1} = \mathbf{N}_{k+1}\boldsymbol{\sigma}_{k+1} \tag{9}$$

the local stress–strain relationships for all PODs i;

$$\mathbf{s}_{i_{k+1}} = \mathbf{D}_{\mathrm{ls}_{i_{k+1}}}\mathbf{e}_{i_{k+1}} \tag{10}$$

$$\mathbf{e}_{\mathrm{f}_{i_{k+1}}} = \mathbf{C}_{\mathrm{lsf}_{i_{k+1}}} \mathbf{s}_{i_{k+1}} \tag{11}$$

the flow rule and plastic parameter,

$$\Delta\boldsymbol{\varepsilon}_{\mathrm{p}} = \frac{\partial G}{\partial \boldsymbol{\sigma}_{k+1}} \Delta\lambda \tag{12}$$

$$\Delta\kappa = X_{k+1} \Delta\lambda \frac{\partial G}{\partial \boldsymbol{\sigma}_{k+1}} \tag{13}$$

and the yield function

$$F(\boldsymbol{\sigma}_{k+1}, \kappa_{k+1}) = 0 \tag{14}$$

The following total–local function is used to ensure (8)–(11) are simultaneously satisfied

$$\mathbf{F}_{\mathrm{e}_{i_{k+1}}} = \mathbf{N}_{i_{k+1}} \boldsymbol{\sigma}_{k+1} - \mathbf{D}_{\mathrm{ls}_{i_{k+1}}} \mathbf{e}_{i_{k+1}} = \mathbf{0} \tag{15}$$

The approach developed is essentially an extension of the Closest Point Projection algorithm (Simo and Hughes, 1998). Error measures are introduced for the plastic strain and plastic parameter, which along with the error in the yield function and total–local function are used in a coupled Newton iterative solution procedure.

For clarity the overall iteration subscripts will now be dropped, it being assumed that all quantities on the right of an equation are those from the previous update iteration (or the values from the previous overall finite element increment for the first iteration).

The plastic strain and hardening parameter errors are defined as follows

$$\mathbf{R}_{\varepsilon} = -\Delta\boldsymbol{\varepsilon}_{\mathrm{p}} + \frac{\partial G}{\partial \boldsymbol{\sigma}} \Delta\lambda \tag{16}$$

$$R_{\kappa} = -\Delta\kappa + X \Delta\lambda \boldsymbol{\sigma}^{\mathrm{T}} \frac{\partial G}{\partial \boldsymbol{\sigma}} \tag{17}$$

From which the iterative corrections are obtained as follows

$$\delta\boldsymbol{\varepsilon}_{\mathrm{p}} = \mathbf{R}_{\varepsilon} + \delta\lambda \frac{\partial G}{\partial \boldsymbol{\sigma}} + \Delta\lambda \frac{\partial^2 G}{\partial \boldsymbol{\sigma}^2} \delta\boldsymbol{\sigma} \tag{18}$$

$$\delta\kappa = a_{\kappa}(R_{\kappa} + \Delta\lambda \mathbf{k}_{\sigma}^{\mathrm{T}} \delta\boldsymbol{\sigma} + c_{\kappa} \delta\lambda) \tag{19}$$

in which

$$a_{\kappa} = \left(1 - \Delta\lambda X \boldsymbol{\sigma}^{\mathrm{T}} \frac{\partial G}{\partial \boldsymbol{\sigma}}\right)^{-1}, \quad c_{\kappa} = X \boldsymbol{\sigma}^{\mathrm{T}} \frac{\partial G}{\partial \boldsymbol{\sigma}} \quad \text{and} \quad \mathbf{k}_{\sigma} = \frac{\partial X}{\partial \boldsymbol{\sigma}} \boldsymbol{\sigma}^{\mathrm{T}} \frac{\partial G}{\partial \boldsymbol{\sigma}} + X \frac{\partial^2 G}{\partial \boldsymbol{\sigma}^2} \boldsymbol{\sigma} + X \frac{\partial G}{\partial \boldsymbol{\sigma}}$$

The yield function consistency condition is written as

$$F + \frac{\partial F^{\mathrm{T}}}{\partial \boldsymbol{\sigma}} \delta\boldsymbol{\sigma} + \frac{\partial F}{\partial \kappa} \delta\kappa = 0 \tag{20}$$

which, making use of (19) and rearranging gives

$$F + \mathbf{f}_{\kappa}^{\mathrm{T}} \delta\boldsymbol{\sigma} + \frac{\partial F}{\partial \kappa} a_{\kappa} R_{\kappa} + h_{\kappa} \delta\lambda = 0 \tag{21}$$

where $\mathbf{f}_{\kappa} = \partial F/\partial\boldsymbol{\sigma} + (\partial F/\partial\kappa) a_{\kappa} \Delta\lambda \mathbf{k}_{\sigma}$ and $h_{\kappa} = (\partial F/\partial\kappa) a_{\kappa} c_{\kappa}$.

The total–local consistency condition is obtained from (15), as follows:

$$\mathbf{F}_{\mathrm{e}_i} + \mathbf{N}_i \delta\boldsymbol{\sigma} + \frac{\partial \mathbf{N}_i}{\partial \boldsymbol{\sigma}} \circ \boldsymbol{\sigma} \delta\boldsymbol{\sigma} - \frac{\partial \mathbf{D}_{\mathrm{ls}_i}}{\partial \mathbf{e}_i} \circ \mathbf{e}_i \delta\mathbf{e}_i - \frac{\partial \mathbf{D}_{\mathrm{ls}_i}}{\partial \kappa} \delta\kappa \mathbf{e}_i - \mathbf{D}_{\mathrm{ls}_i} \delta\mathbf{e}_i = \mathbf{0} \tag{22}$$

in which $\circ$ is used to denote a contraction with respect to the 'in-plane' components of a third order matrix.

Since the POD directions do not change during these stress update iterations, although as explained later they are set within the overall stress update process, the third term is null here. Then, using Eq. (19), (22) may be written

$$\mathbf{F}_{\mathrm{e}_i} + \mathbf{N}_{\Delta_i}\,\delta\boldsymbol{\sigma} - \mathbf{d}_{\kappa_i} a_\kappa (R_\kappa + c_\kappa\,\delta\lambda) - \mathbf{D}_{\mathrm{lt}_i}\delta\mathbf{e}_i = \mathbf{0} \tag{23}$$

where $\mathbf{D}_{\mathrm{lt}_i} = (\partial\mathbf{D}_{\mathrm{ls}_i}/\partial\mathbf{e}_i)\circ\mathbf{e}_i + \mathbf{D}_{\mathrm{ls}_i}$, $\mathbf{d}_{\kappa_i} = (\partial\mathbf{D}_{\mathrm{ls}_i}/\partial\kappa)\mathbf{e}_i$ and $\mathbf{N}_{\Delta_i} = \mathbf{N}_i - \mathbf{d}_{\kappa_i} a_{\kappa_i}\mathbf{k}_{\sigma_i}^{\mathrm{T}}\,\Delta\lambda$.

The first trial stress is given by

$$\boldsymbol{\sigma} = \mathbf{D}_{\mathrm{e}}\left(\boldsymbol{\varepsilon} + \Delta\boldsymbol{\varepsilon} - \boldsymbol{\varepsilon}_{\mathrm{p}} - \sum_{j=1}^{n_{\mathrm{p}}}\mathbf{N}_j^{\mathrm{T}}\mathbf{e}_{\mathrm{f}_j}\right) \tag{24}$$

and thereafter iterations are performed to satisfy Eqs. (8)–(14), throughout which the total strain tensor does not change and thus the iterative change in the stress is given by

$$\delta\boldsymbol{\sigma} = -\mathbf{D}_{\mathrm{e}}\left(\delta\boldsymbol{\varepsilon}_{\mathrm{p}} + \sum_{j=1}^{n_{\mathrm{p}}}\mathbf{N}_j^{\mathrm{T}}\,\delta\mathbf{e}_{\mathrm{f}_j}\right) \tag{25}$$

The iterative change in $\mathbf{e}_{\mathrm{f}}$ is given by

$$\delta\mathbf{e}_{\mathrm{f}_i} = (\mathbf{I} - \mathbf{M}'_{x_i})\,\delta\mathbf{e}_i + \mathbf{m}'_{\kappa_i}\,\delta\kappa \tag{26}$$

where $\mathbf{M}'_x = \mathbf{M}_x + (\partial\mathbf{M}_x/\partial\mathbf{e})\circ\mathbf{e}$ and $\mathbf{m}'_\kappa = (\partial\mathbf{M}_x/\partial\kappa)\mathbf{e}$.

Making use of (18), (19) and (26), Eq. (25) may be rearranged to be

$$\delta\boldsymbol{\sigma} = -\mathbf{A}\left(\mathbf{R}_\varepsilon + \delta\lambda\frac{\partial G}{\partial\boldsymbol{\sigma}} + \sum_{j=1}^{n_{\mathrm{p}}}\mathbf{N}_j^{\mathrm{T}}((\mathbf{I} - \mathbf{M}'_{x_j})\,\delta\mathbf{e}_j + \mathbf{m}'_{\kappa_j}(a_\kappa(R_\kappa + c_\kappa\,\delta\lambda)))\right) \tag{27}$$

in which

$$\mathbf{A} = \left[\mathbf{I} + \mathbf{D}_{\mathrm{e}}\left(\Delta\lambda\frac{\partial^2 G}{\partial\boldsymbol{\sigma}^2} - \sum_{j=1}^{n_{\mathrm{p}}}\mathbf{N}_j^{\mathrm{T}}\mathbf{m}'_{\kappa_j}a_\kappa\mathbf{k}_\sigma^{\mathrm{T}}\,\Delta\lambda\right)\right]^{-1}\mathbf{D}_{\mathrm{e}}$$

Substituting for $\delta\boldsymbol{\sigma}$ from Eq. (27) in both Eqs. (21) and (23) gives a set of coupled equations with $\delta\lambda$ and $\delta\mathbf{e}_i$ as the unknowns. These are written in the following compact form, in which i and j are indices from 1 to n_{p} and in which the summation of repeated indices is implied.

$$\begin{aligned} F_\lambda &= M_\lambda\,\delta\lambda + \mathbf{b}_{\lambda_j}\,\delta\mathbf{e}_j \\ \mathbf{F}_{\mathrm{E}_i} &= \mathbf{m}_{\mathrm{E}_i}\delta\lambda + \mathbf{B}_{\mathrm{E}_{i,j}}\delta\mathbf{e}_j \end{aligned} \tag{28}$$

in which

$$F_\lambda = F - \mathbf{f}_\kappa^{\mathrm{T}}\mathbf{A}\left(\mathbf{R}_\varepsilon - \sum_{k=1}^{n_{\mathrm{p}}}\mathbf{N}_k^{\mathrm{T}}\mathbf{m}'_{\kappa_k}a_\kappa R_\kappa\right) + \frac{\partial F}{\partial\kappa}a_\kappa R_\kappa$$

$$\mathbf{F}_{\mathrm{E}_i} = \mathbf{F}_{\mathrm{e}_i} - \mathbf{N}_{\Delta_i}\mathbf{A}\left(\mathbf{R}_\varepsilon - \sum_{k=1}^{n_{\mathrm{p}}}\mathbf{N}_k^{\mathrm{T}}\mathbf{m}'_{\kappa_k}a_\kappa R_\kappa\right) - \mathbf{d}_{\kappa_i}a_\kappa R_\kappa$$

$$M_\lambda = \mathbf{f}_\kappa^{\mathrm{T}}\mathbf{A}\left(\frac{\partial G}{\partial\boldsymbol{\sigma}} - \sum_{k=1}^{n_{\mathrm{p}}}\mathbf{N}_k^{\mathrm{T}}\mathbf{m}'_{\kappa_k}a_\kappa c_\kappa\right) - h_\kappa$$

$$\mathbf{m}_{\mathrm{E}_i} = \mathbf{N}_{\Delta_i}\mathbf{A}\left(\frac{\partial G}{\partial\boldsymbol{\sigma}} - \sum_{k=1}^{n_{\mathrm{p}}}\mathbf{N}_k^{\mathrm{T}}\mathbf{m}'_{\kappa_k}a_\kappa c_\kappa\right) + \mathbf{d}_{\kappa_i}a_\kappa c_\kappa$$

$$\mathbf{b}_{\lambda_j} = \mathbf{f}_\kappa^{\mathrm{T}} \mathbf{A} \mathbf{N}_j^{\mathrm{T}} (\mathbf{I} - \mathbf{M}'_{x_j})$$

$$\mathbf{B}_{\mathrm{E}_{i,j}} = \mathbf{N}_{\Delta_i} \mathbf{A} \mathbf{N}_j^{\mathrm{T}} (\mathbf{I} - \mathbf{M}'_{x_j}) + \mathbf{D}_{\mathrm{lt}_{i,j}} \partial_{i,j}$$

where $\partial_{i,j}$ in the expression for $\mathbf{B}_{\mathrm{E}}$ is the Kronecker delta.

The overall steps of the return-mapping algorithm may now be summarized for the case when one or more POD exists and there is plastic yield

Box 1. Return-mapping algorithm

Step	Description
1	Initialize $\Delta\lambda = 0$ and $\Delta\kappa = 0$
2	Compute trial stress from (24)
3	Evaluate F_λ, M_λ, $\mathbf{b}_\lambda$, $\mathbf{F}_{\mathrm{E}}$, $\mathbf{m}_{\mathrm{E}}$, $\mathbf{B}_{\mathrm{E}}$ from (28) and solve for $\delta\lambda$ and $\delta\mathbf{e}_i$
4	Compute $\delta\boldsymbol{\sigma}$ from (27)
5	Update $\mathbf{e}_i$ using $\mathbf{e}_i = \mathbf{e}_i + \delta\mathbf{e}_i$ and update ζ_i
6	Compute $\delta\boldsymbol{\varepsilon}_{\mathrm{p}}$, $\delta\kappa$ from (18) and (19) respectively
7	Update plastic terms $\boldsymbol{\varepsilon}_{\mathrm{p}} = \boldsymbol{\varepsilon}_{\mathrm{p}} + \delta\boldsymbol{\varepsilon}_{\mathrm{p}}$, $\Delta\boldsymbol{\varepsilon}_{\mathrm{p}} = \Delta\boldsymbol{\varepsilon}_{\mathrm{p}} + \delta\boldsymbol{\varepsilon}_{\mathrm{p}}$, $\Delta\lambda = \Delta\lambda + \delta\lambda$, $\Delta\kappa = \Delta\kappa + \delta\kappa$ and $\kappa = \kappa + \delta\kappa$
8	Compute a new trial stress from $\boldsymbol{\sigma} = \mathbf{D}_{\mathrm{e}}\left(\boldsymbol{\varepsilon} - \boldsymbol{\varepsilon}_{\mathrm{p}} - \sum_{j=1}^{n_{\mathrm{p}}} \mathbf{N}_j^{\mathrm{T}} (\mathbf{I} - \mathbf{M}_x)\mathbf{e}_j\right)$
9	Compute F and $\mathbf{F}_{\mathrm{e}_i}$, $\mathbf{R}_\varepsilon$, R_κ from (14)–(17) respectively
10	Check for convergence i.e. if $\lvert F\rvert \leqslant \sigma_{\mathrm{tol}}$, $\lvert\mathbf{F}_{\mathrm{e}}\rvert \leqslant \sigma_{\mathrm{tol}}$, $\lvert\mathbf{R}_\varepsilon\rvert \leqslant \varepsilon_{\mathrm{tol}}$ and $R_\kappa \leqslant \varepsilon_{\mathrm{tol}}$ Stop, else return to Step 2 [1]

4. Consistent tangent constitutive relationship

A algorithmic tangent constitutive matrix is now derived which is consistent with the above stress update algorithm. The differential form of Eq. (8) may be written as

$$\mathrm{d}\boldsymbol{\sigma} = \mathbf{D}_{\mathrm{e}}\left(\mathrm{d}\boldsymbol{\varepsilon} - \mathrm{d}\boldsymbol{\varepsilon}_{\mathrm{p}} - \sum_{j=1}^{n_{\mathrm{p}}} \left(\mathbf{N}_j^{\mathrm{T}}\, \mathrm{d}\mathbf{e}_{\mathrm{f}_j} + \mathrm{d}\mathbf{N}_j^{\mathrm{T}} \mathbf{e}_{\mathrm{f}_j}\right)\right) \tag{29}$$

The term $\mathrm{d}\mathbf{N}_i$, which is only non-zero for PODs that have formed since the last converged state, is computed from the differential of the transformation matrix with respect to the trial stress components used for new POD detection. The choice of this stress tensor, denoted $\boldsymbol{\sigma}_{\mathrm{I}}$, is discussed in Section 5. It is important that all new PODs are based on the same $\boldsymbol{\sigma}_{\mathrm{I}}$, and that $\partial\boldsymbol{\sigma}_{\mathrm{I}}/\partial\boldsymbol{\varepsilon} = \mathbf{D}_{\mathrm{I}}$ can be calculated at the constitutive matrix stage of the computation, noting that the subscript I is chosen to denote the POD Initialization stress. Thus Eq. (29) may now be written

$$\mathrm{d}\boldsymbol{\sigma} = \mathbf{D}_{\mathrm{e}}\left(\mathrm{d}\boldsymbol{\varepsilon} - \mathrm{d}\boldsymbol{\varepsilon}_{\mathrm{p}} - \sum_{j=1}^{n_{\mathrm{p}}} \left(\mathbf{N}_j^{\mathrm{T}}\, \mathrm{d}\mathbf{e}_{\mathrm{f}_j} + \frac{\partial \mathbf{N}_j^{\mathrm{T}}}{\partial \boldsymbol{\sigma}_{\mathrm{I}}} \circ \mathbf{e}_{\mathrm{f}_j} \mathbf{D}_{\mathrm{I}}\, \mathrm{d}\boldsymbol{\varepsilon}\right)\right) \tag{30}$$

The computation of the transformation matrix derivatives is potentially computationally expensive, and therefore an efficient procedure is required for their evaluation. Mahnken et al. (2000) used an approach given by Miehe (1993) and here a similar approach is used in that the derivatives have been computed directly

[1] Tolerance levels are $\varepsilon_{\mathrm{tol}} = \varepsilon_t \times 10^{-6}$, $\sigma_{\mathrm{tol}} = f_{\mathrm{t}} \times 10^{-6}$.

from the stress invariant derivatives, although the details of the present approach are somewhat different from that presented by Mahnken et al. (2000). The approach used here is summarized in Appendix A.

Differentiating Eq. (6) yields

$$\mathrm{d}\mathbf{e}_{\mathrm{f}_i} = \mathbf{C}_{\mathrm{ltf}}\,\mathrm{d}\mathbf{s} - \varpi_\kappa\,\mathrm{d}\kappa \tag{31}$$

in which $\mathbf{C}_{\mathrm{ltf}} = (\mathbf{M}_x'^{-1} - \mathbf{I})\mathbf{C}_{\mathrm{L}}$ and $\varpi_\kappa = \mathbf{M}_x'^{-1}\mathbf{m}_\kappa'$.

The differential quantities of the plastic strain, plastic parameter and the local stress vector may be written as follows

$$\mathrm{d}\boldsymbol{\varepsilon}_{\mathrm{p}} = \mathrm{d}\lambda\frac{\partial G}{\partial \boldsymbol{\sigma}} + \Delta\lambda\frac{\partial^2 G}{\partial \boldsymbol{\sigma}^2}\mathrm{d}\boldsymbol{\sigma} \tag{32}$$

$$\mathrm{d}\kappa = a_\kappa(\Delta\lambda\mathbf{k}_\sigma^{\mathrm{T}}\,\mathrm{d}\boldsymbol{\sigma} + c_\kappa\,\mathrm{d}\lambda) \tag{33}$$

$$\mathrm{d}\mathbf{s}_i = \mathbf{N}_i\,\mathrm{d}\boldsymbol{\sigma} + \frac{\partial \mathbf{N}_i}{\partial \boldsymbol{\sigma}_{\mathrm{I}}} \circ \boldsymbol{\sigma}_{\mathrm{I}}\mathbf{D}_{\mathrm{I}}\,\mathrm{d}\boldsymbol{\varepsilon} \tag{34}$$

Using Eqs. (31)–(34) in (30) and rearranging gives

$$\mathrm{d}\boldsymbol{\sigma} = \mathbf{A}_{\mathrm{c}}\left[\left(\mathbf{I} - \sum_{j=1}^{n_{\mathrm{p}}}\left(\mathbf{N}_j^{\mathrm{T}}\mathbf{C}_{\mathrm{ltf}_j}\frac{\partial \mathbf{N}_j}{\partial \boldsymbol{\sigma}_{\mathrm{I}}} \circ \boldsymbol{\sigma}\mathbf{D}_{\mathrm{I}} + \frac{\partial \mathbf{N}_j^{\mathrm{T}}}{\partial \boldsymbol{\sigma}_{\mathrm{I}}} \circ \mathbf{e}_{\mathrm{f}_j}\mathbf{D}_{\mathrm{I}}\right)\right)\mathrm{d}\boldsymbol{\varepsilon} - \left(\frac{\partial G}{\partial \boldsymbol{\sigma}} - \sum_{j=1}^{n_{\mathrm{p}}}\left(\mathbf{N}_j^{\mathrm{T}}\varpi_\kappa a_\kappa c_\kappa\right)\right)\mathrm{d}\lambda\right] \tag{35}$$

in which

$$\mathbf{A}_{\mathrm{c}} = \left[\mathbf{I} + \mathbf{D}_{\mathrm{e}}\left(\sum_{j=1}^{n_{\mathrm{p}}}\mathbf{N}_j^{\mathrm{T}}\mathbf{C}_{\mathrm{ltf}_j}\mathbf{N}_j - \varpi_\kappa a_\kappa\Delta\lambda\mathbf{k}_\sigma^{\mathrm{T}}\right) + \Delta\lambda\frac{\partial^2 G}{\partial \boldsymbol{\sigma}^2}\right]^{-1}\mathbf{D}_{\mathrm{e}}$$

The consistency condition for the yield surface gives

$$\mathrm{d}F = \mathbf{f}_\kappa^{\mathrm{T}}\mathrm{d}\boldsymbol{\sigma} + h_\kappa\mathrm{d}\lambda = 0 \tag{36}$$

Substituting for $\mathrm{d}\boldsymbol{\sigma}$ in Eq. (36) from (35) and rearranging gives

$$\mathrm{d}\lambda = \frac{\mathbf{f}_\kappa^{\mathrm{T}}\mathbf{A}_{\mathrm{c}}\mathbf{I}_N}{\mathbf{f}_\kappa^{\mathrm{T}}\mathbf{A}_{\mathrm{c}}\mathbf{g}_{\mathrm{m}} - h_\kappa}\mathrm{d}\boldsymbol{\varepsilon} \tag{37}$$

in which

$$\mathbf{I}_N = \mathbf{I} - \sum_{j=1}^{n_{\mathrm{p}}}\left(\mathbf{N}_j^{\mathrm{T}}\mathbf{C}_{\mathrm{ltf}_j}\frac{\partial \mathbf{N}_j}{\partial \boldsymbol{\sigma}_{\mathrm{I}}} \circ \boldsymbol{\sigma}\mathbf{D}_{\mathrm{I}} + \frac{\partial \mathbf{N}_j^{\mathrm{T}}}{\partial \boldsymbol{\sigma}_{\mathrm{I}}} \circ \mathbf{e}_{\mathrm{f}_j}\mathbf{D}_{\mathrm{I}}\right) \quad \text{and} \quad \mathbf{g}_{\mathrm{m}} = \frac{\partial G}{\partial \boldsymbol{\sigma}} - \sum_{j=1}^{n_{\mathrm{p}}}\left(\mathbf{N}_j^{\mathrm{T}}\varpi_\kappa a_\kappa c_\kappa\right)$$

Substituting for $\mathrm{d}\lambda$ in Eq. (35) from (37), gives the consistent tangent relationship, as follows

$$\mathrm{d}\boldsymbol{\sigma} = \left[\mathbf{A}_{\mathrm{c}}\mathbf{I}_N - \frac{\mathbf{A}_{\mathrm{c}}\mathbf{g}_{\mathrm{m}}\mathbf{f}_\kappa^{\mathrm{T}}\mathbf{A}_{\mathrm{c}}\mathbf{I}_N}{\mathbf{f}_\kappa^{\mathrm{T}}\mathbf{A}_{\mathrm{c}}\mathbf{g}_{\mathrm{m}} - h_\kappa}\right]\mathrm{d}\boldsymbol{\varepsilon} \tag{38}$$

5. Stress computation procedure

The return-mapping algorithm described in Section 3 is only one component, albeit the major one, of the stress computation procedure. Before the return-mapping algorithm is entered however, decisions have to be made on whether plasticity will occur and whether one or more new POD will form in the current step. These decisions require a trial stress, the natural choice for which would be that given by Eq. (24), which

assumes that the trial stress increment is elastic. However, this was found to be inefficient because in many instances the elastic stress incorrectly predicted yield and POD formation. Therefore an alternative approach of using the secant elastic-damage constitutive matrix was adopted. The trial stress, upon which yield and new POD formation decisions are made, is therefore as shown below,

$$\boldsymbol{\sigma}_{\mathrm{I}} = \left(\mathbf{I} + \mathbf{D}_{\mathrm{e}} \sum_{j=1}^{n} \mathbf{N}_j^{\mathrm{T}} \mathbf{C}_{\mathrm{lsf}_j} \mathbf{N}_j \right)^{-1} \mathbf{D}_{\mathrm{e}} (\boldsymbol{\varepsilon}_k + \Delta\boldsymbol{\varepsilon} - \boldsymbol{\varepsilon}_{\mathrm{p}_k}) = \mathbf{D}_{\mathrm{I}} (\boldsymbol{\varepsilon}_k + \Delta\boldsymbol{\varepsilon} - \boldsymbol{\varepsilon}_{\mathrm{p}_k}) \tag{39}$$

The overall stress recovery procedure systematically checks for the formation of PODs one at a time. The first return-mapping is undertaken with any existing PODs and plastic flow, if required, after which a check is performed for new POD formation. If required, one new POD is formed and the next reduction undertaken and then a further check performed for the next POD. This continues until the POD formation criterion is not violated. This procedure can result in the return-mapping exercise being carried out more then once per analysis step per integration point, however, this systematic approach does avoid spurious POD formation and in a reality the amount of extra computational effort in a full-scale finite element analysis is limited.

Box 2. Overall stress calculation procedure

Step	Description
1	Record all state variables on entry
2	Evaluate $\boldsymbol{\sigma}_{\mathrm{I}}$ from (39)

3	If $F(\boldsymbol{\sigma}_{\mathrm{I}}, \kappa) > 0$ and $I_1(\boldsymbol{\sigma}_{\mathrm{I}}) < 0$ then
	Carry out return-mapping with plasticity and existing PODs to obtain new stress $\boldsymbol{\sigma}$
	IF $\Delta\lambda < 0$, then
	Reset state variables and carryout mapping without plasticity
	End if
	Else
	If ($n_{\mathrm{p}} > 0$) carry out return-mapping with existing PODs to obtain new stress $\boldsymbol{\sigma}$
	Else
	$\boldsymbol{\sigma} = \boldsymbol{\sigma}_{\mathrm{I}}$
	End if

4	For $i = 1$, n_{form}. *Enter POD formation loop* [2]
	IF $\sigma_1(\boldsymbol{\sigma}) > f_{ti}$ then *If major principal stress exceeds formation criterion* [3]
	Form one new POD [4], but using principal direction of $\boldsymbol{\sigma}_{\mathrm{I}}$ nearest that of $\boldsymbol{\sigma}$
	Reset all state variables
	Carryout return-mapping with revised number of PODs to obtain new stress $\boldsymbol{\sigma}$
	Else
	No new PODs, record final stress and exit formation loop
	End if
	End For

[2] n_{form} = Maximum number of PODs permitted to form.

[3] The procedure can also use alternative formation criterion, such as an initial damage function being exceeded.

[4] A POD (j) is only permitted to form if the normal satisfies $\mathbf{r}_{\mathrm{d}_i}^{\mathrm{T}} \mathbf{r}_{\mathrm{d}_j} \leqslant 0.65$, where $i = 1$, n_{p} (with n_{p} being the existing number of PODs).

6. Examples

All of the examples were undertaken with the finite element program LUSAS (FEA Ltd, 2002) in which the current model has been implemented. Quadratic elements were used throughout, which were 6-noded triangular and 8-noded quadrilateral elements for 2D examples and 20-noded hexahedral elements for the 3D example. Full numerical integration was performed for all 2D elements, i.e. 3×3 Gaussian for quadrilateral and 6 point Radau for triangular elements, and Iron's 14 point rule was used for the 20-noded elements (FEA Ltd, 2002).

The standard tolerance adopted for convergence of the incremental iterative solutions was 10^{-4} for both the out of balance force (ψ_f) and iterative displacement (ψ_u), norms, which are defined below

$$\psi_f = \frac{\sqrt{\boldsymbol{\psi}_r^T \boldsymbol{\psi}_r}}{\sqrt{\boldsymbol{\psi}_T^T \boldsymbol{\psi}_T}} \tag{40}$$

and

$$\psi_u = \frac{\sqrt{\boldsymbol{\psi}_\delta^T \boldsymbol{\psi}_\delta}}{\sqrt{\boldsymbol{\psi}_{uT}^T \boldsymbol{\psi}_{uT}}} \tag{41}$$

in which $\boldsymbol{\psi}_r$ is the vector of nodal residual forces, $\boldsymbol{\psi}_T$ is the total nodal force vector, $\boldsymbol{\psi}_\delta$ is the vector of iterative nodal displacements and $\boldsymbol{\psi}_{uT}$ is the vector of total nodal displacements.

It is noted, however, that a more stringent tolerance was used for the convergence study in Example 1.

The solutions all employed an automatic step selection procedure in which the displacement or load increment is adjusted according to the number of iterations taken to achieve convergence in the previous step. The standard number of target iterations was set between 3 and 5 and the maximum number of iterations permitted before automatic step reduction was set to between 7 and 9. In some cases this automatic step selection procedure was linked Crisfield's arc-length method (Crisfield, 1981) in which the product of iterative nodal displacements is constrained to an arc (FEA Ltd, 2002).

As mentioned in the associated paper, the end of the damage softening curve is computed from the characteristic element length and specific fracture energy for all the plain concrete fracture examples.

The only variation from the fixed parameters described in the associated paper, is that the residual damage factor r_c has been set to 0.05 here, rather than 0.01.

6.1. Direct fracture example

The first example presents results from two plane stress analyses of a fracture test specimen example. The un-reinforced fracture specimen was tested by Petersson (1981) and was loaded in direct tension under displacement control. The dimensions of the specimen and two finite element meshes are shown in Fig. 1, and the material properties are shown in Table 1.

The automatic step size procedure was used but with an upper limit of 0.01 mm placed on the prescribed boundary displacement increment. Here the target number of iterations was set to 3 and the convergence tolerance to 10^{-6} for both displacement and residual force norms. This tolerance is relatively small and is considered smaller than necessary, however a tight tolerance is used in this example to demonstrate the convergence properties of the consistent algorithm.

The experimental and numerical load displacement responses are shown in Fig. 2, along with a crack plot for the coarser mesh at the opening displacement marked. The load–displacement graphs obtained

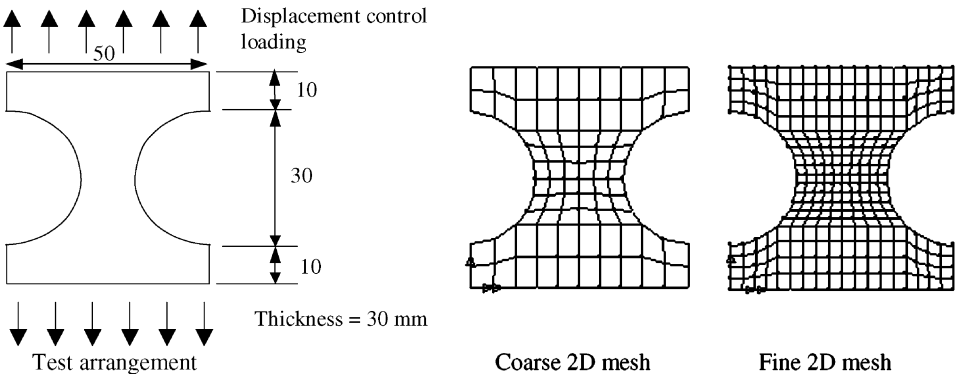

Fig. 1. Example 1. Test arrangement and F.E. meshes.

Table 1
Material properties

Example	E (kN/mm^2)	ν	f_c (N/mm^2)	f_t (N/mm^2)	ε_c	ε_0	G_f (N/mm)	b_c	Z_0	ψ	m_g	m_{ful}
1	35	0.2	40	3.35	0.0022	–	0.10	1.15	0.6	−0.1	0.5	5
2	30	0.2	50	2.6	0.0025	–	0.103	1.15	0.6	−0.1	0.5	5
3	24.5	0.18	35	2.9	0.0022	–	0.10	1.15	0.6	−0.1	0.5	3
4	33	0.2	37	3.1	0.0022	–	0.10	1.15	0.6	−0.1	0.6	3
5	25	0.2	22.6	2.5	0.0022	0.004	–	1.15	0.6	−0.1	0.5	10

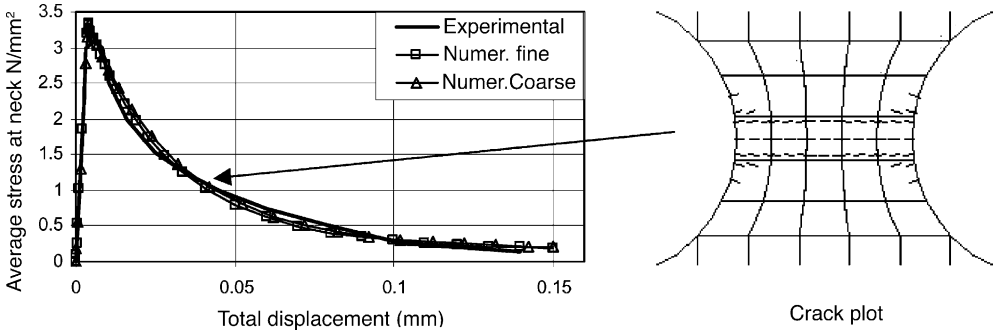

Fig. 2. Example 1. Load–deflection response and crack plot.

using the two meshes are very close to one another and show that the calculation of the characteristic length according to the element size is appropriate.

Details of the analysis solution history are given for the coarse mesh case in Table 2. The history from the fine mesh solution is very similar and therefore only the coarse mesh solution details are provided. It may be seen that the automatic step adjustment procedure and the consistent algorithm produce very good convergence with respect to both iterative displacements and out of balance force residuals.

6.2. Cylindrical notched fracture beam

The second example presents results from a three-dimensional analysis of a cylindrical notched beam. The un-reinforced specimen, tested by Jefferson and Barr (1995), was loaded via a shaped yoke with the

Table 2
Convergence history for Coarse mesh Example 1

Incr	Iter	Total disp. factor	ψ_u	ψ_f
1	0	2.00E−03	1.0000	2.89E−11
1	1		1.13E−15	1.12E−14
2	0	6.00E−03	6.67E−01	2.24E−14
2	1		7.15E−16	8.03E−15
3	0	1.40E−02	5.71E−01	1.81E−14
3	1		6.22E−16	1.01E−14
4	0	3.00E−02	5.33E−01	3.63E−02
4	1		2.77E−03	8.41E−03
4	2		4.40E−04	3.55E−05
4	3		7.15E−07	6.41E−10
5[1]	0	3.46E−02	1.33E−01	9.86E−02
5	1		9.23E−03	5.81E−02
5	2		1.61E−03	7.29E−03
5	3		2.83E−04	1.87E−05
5	4		4.30E−07	4.50E−10
6	0	3.92E−02	1.21E−01	7.06E−02
6	1		6.57E−03	9.18E−02
6	2		3.99E−03	7.53E−03
6	3		5.44E−05	5.13E−07
6	4		2.35E−08	6.65E−14
7	0	4.39E−02	1.19E−01	5.03E−03
7	1		1.24E−04	6.85E−06
7	2		1.46E−06	2.77E−11
7	3		7.53E−13	1.27E−14
8	0	4.92E−02	1.21E−01	3.82E−03
8	1		1.13E−04	3.48E−06
8	2		6.22E−07	5.10E−12
9	0	5.67E−02	1.47E−01	4.50E−03
9	1		1.51E−04	4.00E−06
9	2		5.73E−07	4.52E−12
10	0	6.74E−02	1.72E−01	5.19E−03
10	1		1.92E−04	4.11E−06
10	2		4.46E−07	3.10E−12
11	0	8.25E−02	1.96E−01	5.89E−03
11	1		2.38E−04	3.72E−06
11	2		2.84E−07	1.60E−12
12	0	1.04E−01	2.18E−01	6.87E−03
12	1		3.02E−04	3.03E−06
12	2		1.45E−07	6.28E−13
13	0	1.34E−01	2.35E−01	9.17E−03
13	1		3.91E−04	2.29E−06
13	2		6.08E−08	1.97E−13
14	0	1.77E−01	2.50E−01	1.52E−02
14	1		4.96E−04	1.56E−06
14	2		2.42E−08	1.04E−13

(*continued on next page*)

Table 2 (*continued*)

Incr	Iter	Total disp. factor	ψ_u	ψ_f
15	0	2.37E−01	2.61E−01	2.87E−02
15	1		5.96E−04	1.12E−06
15	2		2.07E−08	1.22E−13
16	0	3.22E−01	2.69E−01	5.70E−02
16	1		6.60E−04	2.05E−06
16	2		2.50E−08	3.34E−13
17	0	4.22E−01	2.39E−01	7.38E−02
17	1		4.86E−04	1.83E−06
17	2		1.26E−08	4.89E−13
18	0	5.22E−01	1.93E−01	6.53E−02
18	1		2.71E−04	7.98E−07
18	2		3.42E−09	4.55E−13
19	0	6.22E−01	1.62E−01	6.42E−02
19	1		1.59E−04	3.76E−07
19	2		9.91E−10	6.96E−13
20	0	7.22E−01	1.39E−01	7.04E−02
20	1		9.62E−05	1.12E−06
20	2		3.22E−10	1.52E−12
21	0	8.22E−01	1.22E−01	4.20E−02
21	1		6.09E−05	3.60E−07
21	2		1.15E−10	1.93E−12
22	0	9.22E−01	1.09E−01	3.52E−02
22	1		3.90E−05	2.33E−07
22	2		4.17E−11	2.42E−12
23	0	1.02E+00	9.80E−02	1.16E−01
23	1		2.56E−05	1.09E−06
23	2		6.70E−11	2.91E−12
24	0	1.12E+00	8.92E−02	2.34E−02
24	1		1.68E−05	9.66E−08
24	2		6.90E−12	3.59E−12
25	0	1.22E+00	8.19E−02	1.86E−02
25	1		1.12E−05	6.07E−08
25	2		3.14E−12	3.37E−12
26	0	1.32E+00	7.57E−02	1.46E−02
26	1		7.57E−06	3.75E−08
26	2		1.53E−12	7.74E−12
27	0	1.42E+00	7.03E−02	2.61E−02
27	1		5.39E−06	4.66E−08
27	2		1.46E−12	7.57E−12
28[2]	0	1.50E+00	5.18E−02	5.26E−03
28	1		2.22E−06	5.23E−09
28	2		3.06E−13	6.78E−12

Notes: (1) 1 failed step and then a step adjustment between increments 4 and 5. (2) Final increment governed by max. prescribed displacement.

Iter Iteration numbers, noting 1st iteration has number 0 Iincs = increment number.

Total Step factor relative to a prescribed displacement of 0.1 mm.

load level being controlled by feedback from a clip gauge at the notch tip. The specimen was supported on curved cradles, as shown in Fig. 3. The material properties are shown in Table 1 and the mesh, which makes use of double symmetry, is illustrated in Fig. 4. In the finite element model the load was applied as a uniform load on the curved surface above the notch, as shown in Fig. 4, with Crisfield's arc-length being employed to allow softening to be simulated. It is noted that because symmetry is used the actual value of G_f used in the analysis is 1/2 of that quoted in the material properties table, since the simulated fracture process zone width is twice that modeled.

The experimental and numerical load displacement responses are shown in Fig. 5 for both the crack mouth opening displacement, which is actually the notch mouth opening here, and the central deflection.

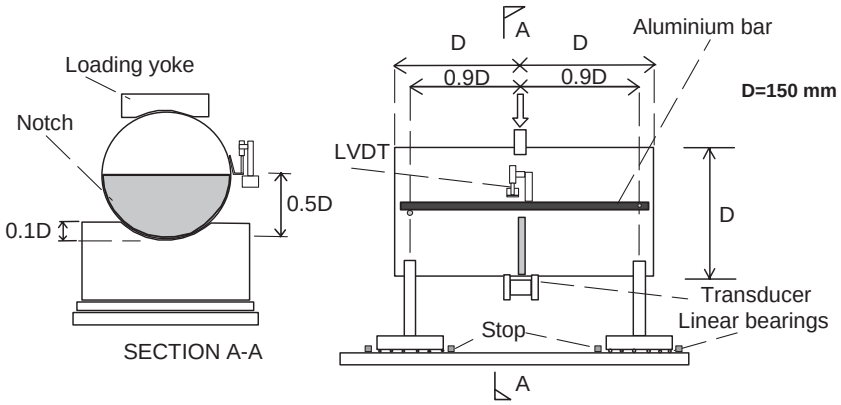

Fig. 3. Example 2. Experimental arrangement of notched cylinder.

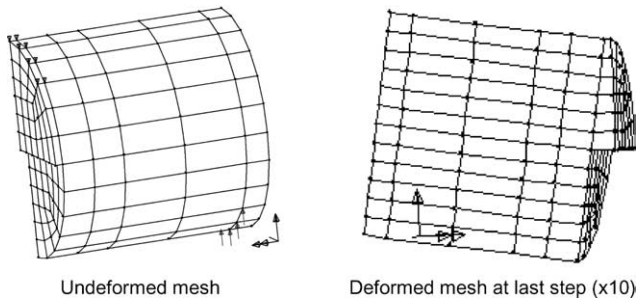

Fig. 4. Example 2. Finite element meshes.

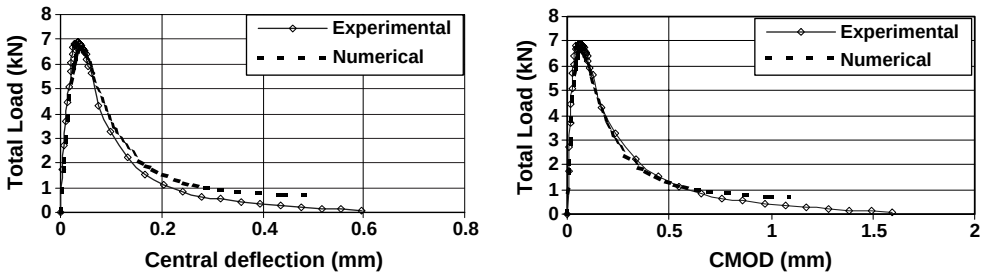

Fig. 5. Example 2. Numerical and experimental response.

The deformed mesh is given in Fig. 4 and this shows that strains localize in the material above the notch, as would be expected for such a test. The agreement between the numerical and experimental responses is generally good.

42 steps were used in the solution, with an average of 4 iterations per step, and during the solution the step size was automatically reduced twice when convergence was not achieved in the maximum number of iterations per increment (8 in this case).

6.3. Single edged notch beam

This single edge notch beam test by Arrea and Ingraffea (1982) has been used by a number of researchers to assess their models (e.g. Rots and de Borst, 1987; Rots, 1988; Tano et al., 1998) and has been used to show crack path sensitivity to the orientation of element local coordinate systems. The testing arrangement and mesh used for the analysis are both shown in Fig. 6 and the material properties are given in Table 1.

As with the previous example, this analysis was undertaken using Crisfield's arc-length method, and the main load was applied in a patch on the upper edge, as illustrated in Fig. 6. About 50 steps were used in the solution with an average of 4 iterations per increment. Four times during the analysis the step size was reduced when convergence was not achieved within the maximum number of iterations, which was 8 in the present case.

The results are shown in Fig. 7 which gives a load verses crack mouth sliding displacement graph, a magnified deformed mesh plot at the final step, as well as crack plots at intermediate and final steps. The initial response is a little less stiff than that observed in the experiment but this was also found by others (for example Rots, 1988). In this example no attempt has been made to repeat the crack path mesh dependence studies conducted by others, but rather the aim here is to show that, with a reasonably fine mesh, the constitutive model does lead to the prediction of a curved crack with softening down to a relatively small proportion of the peak load. It is acknowledged however that the predicted crack path is not as curved as that observed in the experiment. The present analysis was stopped at 50 steps and throughout maintained good convergence and satisfied the standard convergence tolerance of 10^{-4}.

6.4. Displacement controlled shear-tension tests of Nooru-Mohamed

Certain of Nooru-Mohamed's tests have been considered by others with numerical simulations (for example Jirasek and Zimmermann, 1997 and Ožbolt et al., 2002), but the final series reported in his thesis has received little attention from numerical analysts and it is this series, in which both normal and shear displacements were controlled via computer controlled feedback loops, that is considered here. In this

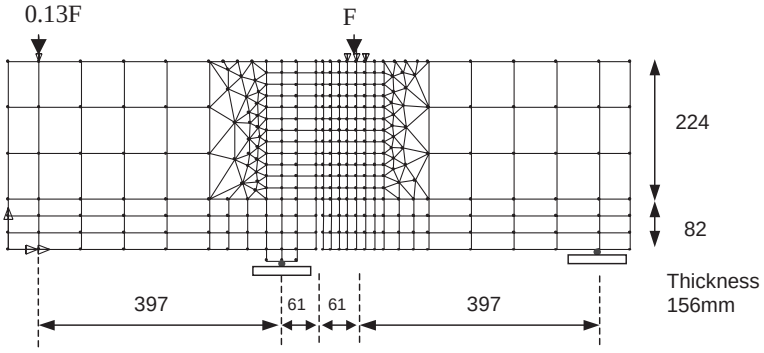

Fig. 6. Example 3. SEN beam by Arrea and Ingraffea, test arrangement and mesh.

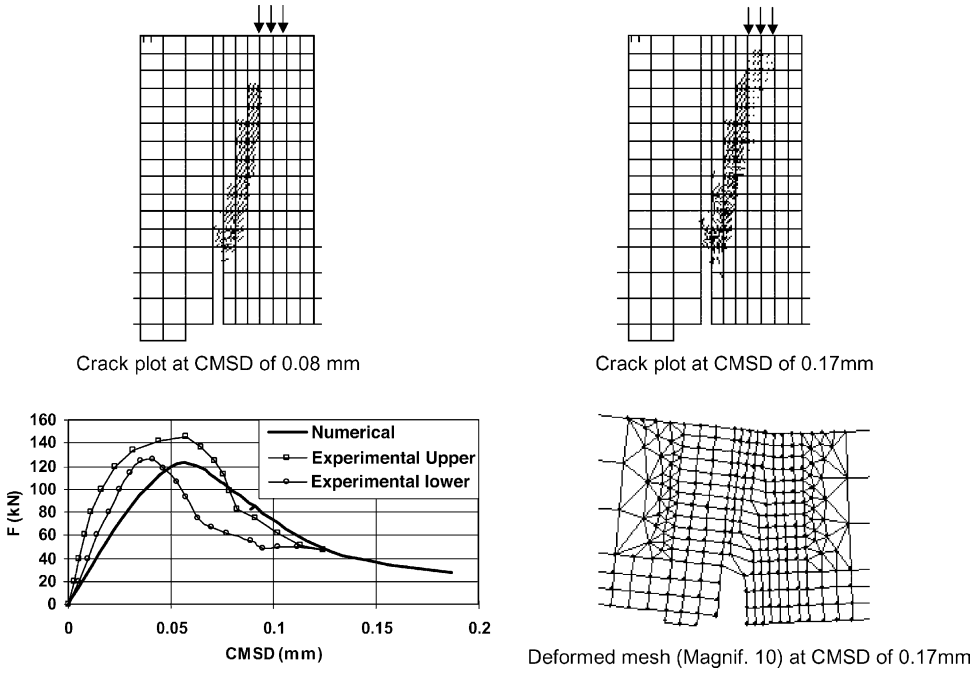

Fig. 7. Example 3. SEN analysis results.

series, tests were conducted with three normal to shear displacement ratios (u/v) of 1, 2 and 3, which were denoted 6a, 6b and 6c respectively by Nooru-Mohamed and here simulations are carried out for all three ratios. The experimental set-up and finite element mesh are illustrated in Fig. 8.

Comparisons between the experimental and numerical load displacement responses are shown in Fig. 9. Fig. 10 shows crack plots, major principal strain contour plots and deformed meshes at the final step of each analysis. The major principal strain plots are included because they provide a good visualization of where major cracking occurred, since this is not provided by the rather diffuse crack plots of 6a and 6b, in which no distinction is made between slightly and heavily damaged PODs.

It is noted that the experimental response given here for 6a is the average of the two tests reported by Nooru-Mohamed, whereas for 6b and 6c only one test was reported for each displacement ratio.

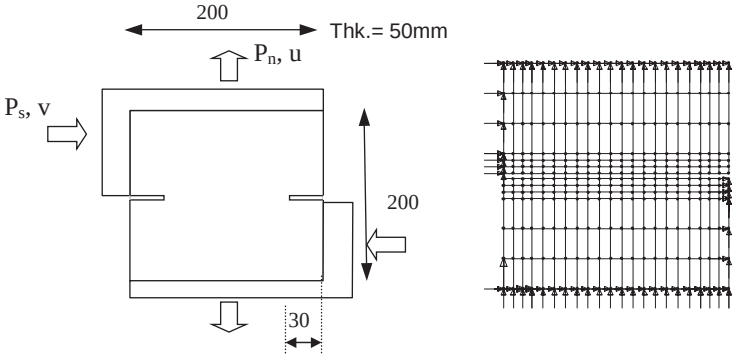

Fig. 8. Example 4. Shear-tension tests by Nooru-Mohamed, test arrangement and mesh.

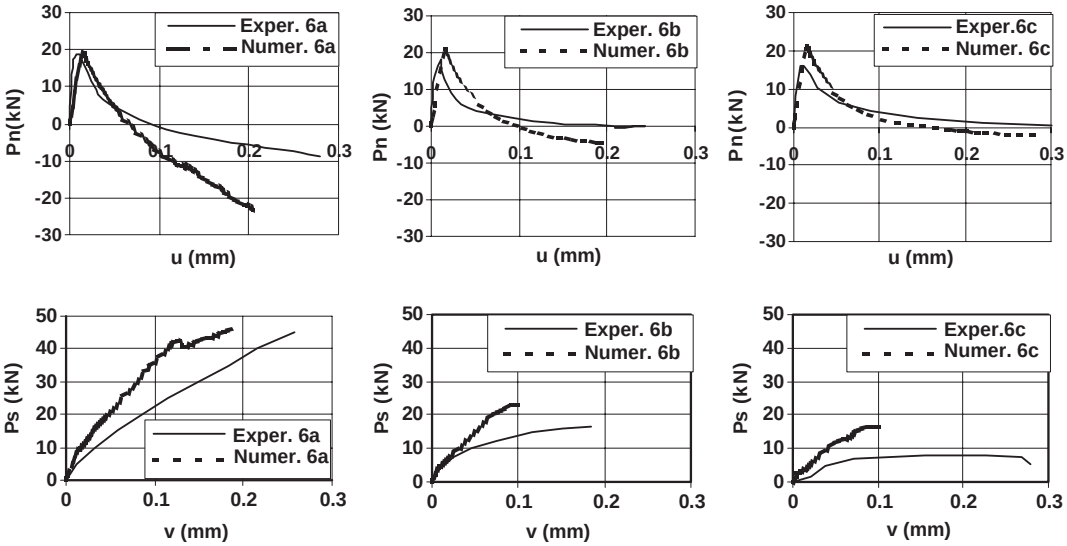

Fig. 9. Example 4. Load–displacement responses.

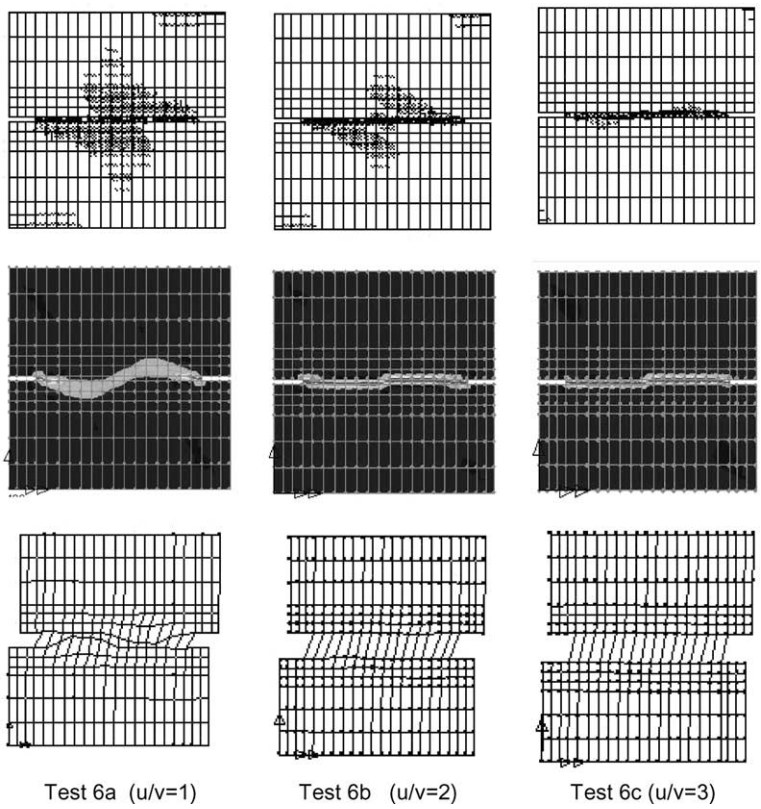

Fig. 10. Example 4. Deformed meshes (10×), localized strain and crack plots at final steps.

The number of steps to achieve the solutions shown varied from 50 to 80 and the number of steps with automatic reductions varied from 5 to 7. The target number of iterations was set to 3 and the limit before automatic step reduction to 8, in all three analyses.

Fig. 9 shows significant discrepancies between numerical and experimental responses, with numerical compressive and shear forces in post-cracking regions generally being higher than the experimental. However, the characteristics of the experimental and numerical responses and the trends with respect to increasing u/v ratios are similar.

The contact functions were developed for the present model from the work of Walraven and Reinhardt (1981) (Jefferson, 2003), with a parameter that reflects the maximum aggregate size. It seems that these functions and the single contact parameter are not able to closely reflect the behavior of Nooru-Mohamed's tests. However, since the trends and characteristics of the numerical response are consistent with those from these experiments and because this type of test is noted for its variability (see Nooru-Mohamed, 1992 and Hassanzadeh, 1991), it is tentatively concluded that this study does demonstrate that the model can represent shear normal behavior, when post-cracking shear contact is significant.

6.5. Reinforced concrete beam by Bresler and Scordelis

The final example is the analysis of a rectangular reinforced concrete beam tested by Bresler and Scordelis (1963). This beam has been used over many years as a test for numerical models for concrete (ASCE, 1982). The aims of including it here are firstly to evaluate the relative effect of including post-damage contact in the constitutive model for a full-scale reinforced concrete case and secondly to include an example in which concrete crushing plays a significant role. The former aim was realised by analysing the beam once using the standard Craft model and then reanalysing it using a damage only (DO) version of model, in which the effects of post-crack contact were not included. In terms of the model equations this was achieved by setting the H_f function to zero.

The experimental details of the beam, along with the finite element mesh used for the analysis, are shown in Fig. 11 and the material properties for the test are given in Table 1.

The standard analysis used 48 steps, the target number of iterations per step was 5 and the maximum number, before automatic step reduction, set to 9. Step reduction occurred 9 times in the solution. It may be

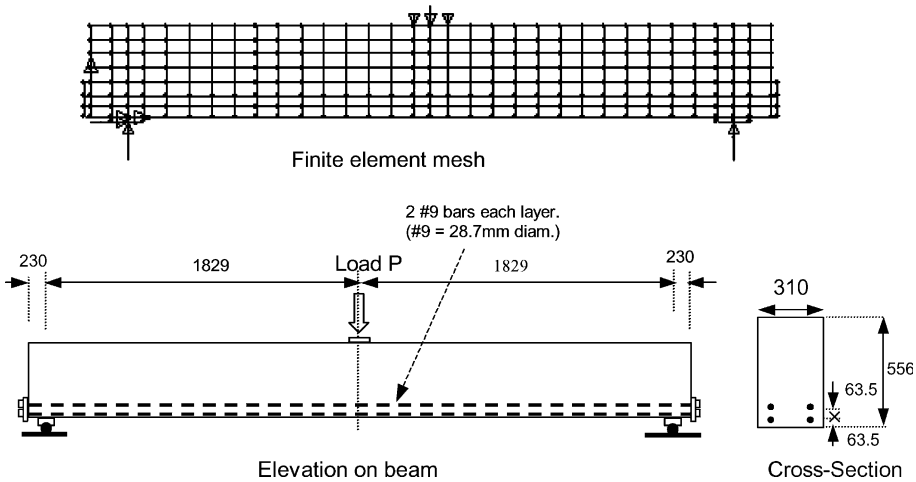

Fig. 11. Example 5. Test arrangement and FE mesh for beam by Bresler and Scordelis.

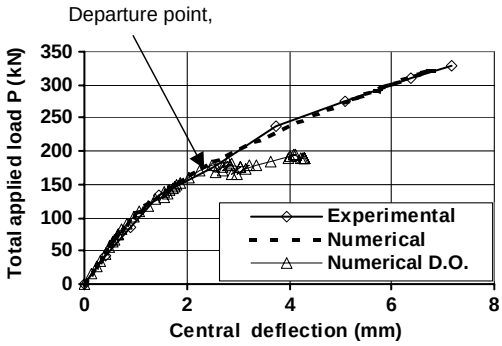

Fig. 12. Example 5. Load–displacement responses.

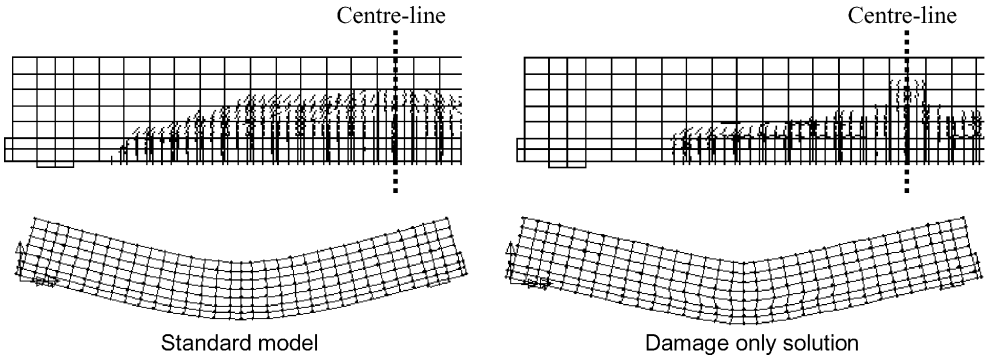

Fig. 13. Example 5. Deformed meshes (10×) and crack plots at final steps.

seen from Fig. 12 that the numerical response is in close agreement with the experimental response and the predicted peak load is within 2% of the experimental peak. A deformed mesh plot and crack plot, which shows widespread diffuse cracking, are shown in Fig. 13. At the final load step the concrete at the top of the section in the central region of the beam had reached the compressive strength limit.

The numerical behavior obtained using the DO and standard models were very similar up to a 'departure point', which is indicated on Fig. 12. In order to get the DO analysis to progress beyond this point it was necessary to use a slacker residual force tolerance of 0.01. Furthermore, an arc-length solution was employed since there was a degree of overall softening. From the deformed mesh plot and crack plots it may be seen that in the DO analysis the model predicts a horizontal shear failure in the concrete above the second line of reinforcing bars; this occurs prior to the overall flexural failure at mid-span. This is considered reasonable since, without Interlock, the shear transfer mechanism is much reduced. The peak load in the DO case is 190 kN, which compares with 322 kN obtained using for the normal model. For this case, therefore, aggregate interlock contributed 41% to the overall strength of the beam, which is within the traditionally suggested limits of 30–60% (ACI-ASCE Committee, 426, 1973).

7. Concluding remarks

The paper has described an overall strategy for the computation of stresses for a plastic-damage-contact model, a part of which was a description of a return-mapping algorithm which fully couples plastic flow to

directional damage and ensures that local and global damage constitutive relationships and the plastic yield condition are all simultaneously satisfied. Furthermore, a tangent constitutive matrix was derived which is consistent with the return-mapping algorithm.

The implementation of the Craft model using the above computational strategy was evaluated in a series of numerical examples. A convergence study was reported for a direct tension fracture test that provided insight into the performance of the consistent algorithmic strategy and served also to validate it. Further fracture examples demonstrated the ability of the model to simulate a range of behavior from plain concrete tests, whilst throughout satisfying relatively stringent convergence tolerances and providing simulations in reasonable agreement with experimental results.

One of the key new aspects of the model, which uses contact theory to represent crack closure and aggregate interlock, was demonstrated in a set of analyses based on the shear-normal test series of Nooru-Mohamed, in which aggregate interlock plays a significant role. Whilst not all of the numerical results were in close agreement with the experimental data, the overall trends of behavior were consistent with the experiments. From this study it was tentatively concluded that the model correctly represented the main characteristics of post-crack shear normal behavior, including situations in which post-crack shear contact is significant.

In a final example the model was tested using a reinforced concrete problem in which crushing and aggregate interlock were both significant. It was shown that the model performs well and provides solutions consistent with the experimental data. Furthermore, the relative contribution of aggregate interlock was explored by removing this component from the model, and it was shown that the peak load was 41% lower without aggregate interlock.

Finally it is concluded that the Craft model, implemented in a finite element program with the proposed return-mapping and consistent tangent matrix algorithms gives reasonable, and often accurate, simulations of a range of plain and reinforced concrete specimens, with solutions that exhibit good convergence properties.

Acknowledgements

I would like to thank the Royal Society (UK) for supporting this work and the finite element software company FEA Ltd. for their support, help and enthusiasm for the work.

Appendix A. Stress transformation matrix derivatives

The form of the transformation matrix was given in the associated paper Jefferson (2003). The principal stresses are given by

$$\sigma_{\mathrm{I}} = \frac{2}{\sqrt{3}}\sqrt{J_2}\cos\left(\theta + 2k\frac{\pi}{3}\right) + \frac{I_1}{3} \tag{A.1}$$

in which, I is the principal stress number, and $k = 0, -1, +1$ for $I = 1, 2, 3$ respectively. I_1, is the first stress invariant, J_2 the second deviatoric invariant and angle θ the Lode angle.

A convenient relationship between the principal stress derivatives and the eigenvector components is as follows

$$\mathbf{N}_1 = \begin{bmatrix} r_{\mathrm{d}_1}^2 & r_{\mathrm{d}_2}^2 & r_{\mathrm{d}_3}^2 & 2r_{\mathrm{d}_1}r_{\mathrm{d}_2} & 2r_{\mathrm{d}_2}r_{\mathrm{d}_3} & 2r_{\mathrm{d}_1}r_{\mathrm{d}_3} \end{bmatrix} = \frac{\partial \sigma_{\mathrm{I}}}{\partial \boldsymbol{\sigma}} \tag{A.2}$$

where $\mathbf{N}_1$ denotes the first row of $\mathbf{N}$.

The principal stress derivatives can be computed from (A.3), as follows

$$\frac{\partial \sigma_{\mathrm{I}}}{\partial \boldsymbol{\sigma}} = c_1 \mathbf{a}_1 + c_2 \mathbf{a}_2 + c_3 \mathbf{a}_3 \tag{A.3}$$

in which

$$\mathbf{a}_1 = \frac{\partial I_1}{\partial \boldsymbol{\sigma}}, \quad \mathbf{a}_2 = \frac{\partial J_2}{\partial \boldsymbol{\sigma}}, \quad \mathbf{a}_3 = \frac{\partial J_3}{\partial \boldsymbol{\sigma}}, \quad c_1 = \frac{1}{3}, \quad c_2 = \frac{A(\theta)}{\sqrt{3J_2}} + \frac{3\mathrm{d}A(\theta)}{2\sin(3\theta)J_2^2} J_3, \quad c_3 = \frac{-\mathrm{d}A(\theta)}{J_2 \sin(3\theta)}$$

$A(\theta) = \cos(\theta)$ if $I = 1$, $A(\theta) = 0.5(-\cos(\theta) + \sqrt{3}\sin(\theta))$ if $I = 2$ and $A(\theta) = -0.5(\cos(\theta) + \sqrt{3}\sin(\theta))$ if $I = 3$ and $\mathrm{d}A(\theta) = \mathrm{d}A/\mathrm{d}\theta$.

The components of $\mathbf{r}_{\mathrm{d}}$ can be computed from (A.2) but it is noted that special provision is required when J_2 is equal or near zero and also when θ is near or equal to 0 or $\pi/3$.

The second differential of principal stresses is used to derive the eigenvector derivatives, as follows:

$$\frac{\partial r_{\mathrm{d}_j}}{\partial \boldsymbol{\sigma}} = \frac{1}{2r_{\mathrm{d}_j}} \left[\frac{\partial^2 \sigma_{\mathrm{I}}}{\partial \boldsymbol{\sigma}^2} \right]^{<j>} \quad \text{if } |r_{\mathrm{d}_j}| \neq 0, \quad \text{otherwise} \quad \frac{\partial r_{\mathrm{d}_j}}{\partial \boldsymbol{\sigma}} = \frac{1}{2r_{\mathrm{d}_k}} \left[\frac{\partial^2 \sigma_{\mathrm{I}}}{\partial \boldsymbol{\sigma}^2} \right]^{<\ell>} \tag{A.4}$$

where the indices j, k and ℓ sequentially take the values

$$j = [1 \quad 2 \quad 3], \quad k = [2 \quad 1 \quad 3] \quad \text{and} \quad \ell = [4 \quad 4 \quad 5] \quad \text{or}$$
$$j = [1 \quad 2 \quad 3], \quad k = [3 \quad 3 \quad 1] \quad \text{and} \quad \ell = [6 \quad 5 \quad 6],$$

the second combination being used when a zero component is encountered in the denominator.

The process for deriving the shear directions $\mathbf{s}_{\mathrm{d}}$ and $\mathbf{t}_{\mathrm{d}}$ was discussed in the associated paper, and the computation will be illustrated for one particular choice of the s direction, i.e.

$$\mathbf{s}_{\mathrm{d}} = \frac{1}{\sqrt{r_{\mathrm{d}_1}^2 + r_{\mathrm{d}_2}^2}} \begin{bmatrix} -r_{\mathrm{d}_2} \\ r_{\mathrm{d}_1} \\ 0 \end{bmatrix} \tag{A.5}$$

Noting that $\mathbf{t}_{\mathrm{d}} = \mathbf{r}_{\mathrm{d}} \times \mathbf{s}_{\mathrm{d}}$, the stress derivatives of $\mathbf{s}_{\mathrm{d}}$ and $\mathbf{t}_{\mathrm{d}}$ are then obtained as follows:

$$\frac{\partial \mathbf{s}_{\mathrm{d}}}{\partial \boldsymbol{\sigma}} = \frac{\partial \mathbf{s}_{\mathrm{d}}}{\partial \mathbf{r}_{\mathrm{d}}} \frac{\partial \mathbf{r}_{\mathrm{d}}}{\partial \boldsymbol{\sigma}} \quad \text{and} \quad \frac{\partial \mathbf{t}_{\mathrm{d}}}{\partial \boldsymbol{\sigma}} = \frac{\partial \mathbf{t}_{\mathrm{d}}}{\partial \mathbf{r}_{\mathrm{d}}} \frac{\partial \mathbf{r}_{\mathrm{d}}}{\partial \boldsymbol{\sigma}} + \frac{\partial \mathbf{t}_{\mathrm{d}}}{\partial \mathbf{s}_{\mathrm{d}}} \frac{\partial \mathbf{s}_{\mathrm{d}}}{\partial \boldsymbol{\sigma}} \tag{A.6}$$

where

$$\frac{\partial \mathbf{s}_{\mathrm{d}}}{\partial \mathbf{r}_{\mathrm{d}}} = \frac{-1}{(r_{\mathrm{d}_1}^2 + r_{\mathrm{d}_2}^2)^{3/2}} \begin{bmatrix} -r_{\mathrm{d}_2} r_{\mathrm{d}_1} & -r_{\mathrm{d}_1}^2 & 0 \\ r_{\mathrm{d}_1}^2 & r_{\mathrm{d}_2} r_{\mathrm{d}_1} & 0 \\ 0 & 0 & 0 \end{bmatrix} + \frac{1}{\sqrt{r_{\mathrm{d}_1}^2 + r_{\mathrm{d}_2}^2}} \begin{bmatrix} 0 & -1 & 0 \\ 1 & 0 & 0 \\ 0 & 0 & 0 \end{bmatrix}$$

$$\frac{\partial \mathbf{t}_{\mathrm{d}}}{\partial \mathbf{r}_{\mathrm{d}}} = \begin{bmatrix} 0 & s_{\mathrm{d}_3} & -s_{\mathrm{d}_2} \\ -s_{\mathrm{d}_3} & 0 & s_{\mathrm{d}_1} \\ s_{\mathrm{d}_2} & -s_{\mathrm{d}_1} & 0 \end{bmatrix} \quad \text{and} \quad \frac{\partial \mathbf{t}_{\mathrm{d}}}{\partial \mathbf{s}_{\mathrm{d}}} = \begin{bmatrix} 0 & -r_{\mathrm{d}_3} & r_{\mathrm{d}_2} \\ r_{\mathrm{d}_3} & 0 & -r_{\mathrm{d}_1} \\ -r_{\mathrm{d}_2} & r_{\mathrm{d}_1} & 0 \end{bmatrix}$$

The derivative of **N** may now be expressed as follows

$$\frac{\partial \mathbf{N}}{\partial \boldsymbol{\sigma}} = \begin{bmatrix} 2r_{d_1}\,dr_{1\sigma} & (s_{d_1}\,dr_{1\sigma} + r_{d_1}\,ds_{1\sigma}) & (t_{d_1}\,dr_{1\sigma} + r_{d_1}\,dt_{1\sigma}) \\ 2r_{d_2}\,dr_{2\sigma} & (s_{d_2}\,dr_{2\sigma} + r_{d_2}\,ds_{2\sigma}) & (t_{d_2}\,dr_{2\sigma} + r_{d_2}\,dt_{2\sigma}) \\ 2r_{d_3}\,dr_{3\sigma} & (s_{d_3}\,dr_{3\sigma} + r_{d_3}\,ds_{3\sigma}) & (t_{d_3}\,dr_{3\sigma} + r_{d_3}\,dt_{3\sigma}) \\ 2(r_{d_2}\,dr_{1\sigma} + r_{d_1}\,dr_{2\sigma}) & (s_{d_2}\,dr_{1\sigma} + s_{d_1}\,dr_{2\sigma} + r_{d_2}\,ds_{1\sigma} + r_{d_1}\,ds_{2\sigma}) & (t_{d_2}\,dr_{1\sigma} + t_{d_1}\,dr_{2\sigma} + r_{d_2}\,dt_{1\sigma} + r_{d_1}\,dt_{2\sigma}) \\ 2(r_{d_3}\,dr_{2\sigma} + r_{d_2}\,dr_{3\sigma}) & (s_{d_3}\,dr_{2\sigma} + s_{d_2}\,dr_{3\sigma} + r_{d_3}\,ds_{2\sigma} + r_{d_2}\,ds_{3\sigma}) & (t_{d_3}\,dr_{2\sigma} + t_{d_2}\,dr_{3\sigma} + r_{d_3}\,dt_{2\sigma} + r_{d_2}\,dt_{3\sigma}) \\ 2(r_{d_3}\,dr_{1\sigma} + r_{d_1}\,dr_{3\sigma}) & (s_{d_3}\,dr_{1\sigma} + s_{d_1}\,dr_{3\sigma} + r_{d_3}\,ds_{1\sigma} + r_{d_1}\,ds_{3\sigma}) & (t_{d_3}\,dr_{1\sigma} + t_{d_1}\,dr_{3\sigma} + r_{d_3}\,dt_{1\sigma} + r_{d_1}\,dt_{3\sigma}) \end{bmatrix}^{\mathrm{T}} \tag{A.7}$$

where $dr_{1\sigma} = \partial r_{d_1}/\partial \boldsymbol{\sigma}$, $ds_{1\sigma} = \partial s_{d_1}/\partial \boldsymbol{\sigma}$ etc.

References

ACI-ASCE Committee 426, 1973. The shear strength of reinforced concrete members. J. Struct. Div. 99 (6).

Arrea, M., Ingraffea, A.R., 1982. Mixed-mode crack propagation in mortar and concrete. Report No. 81-13. Department of Structural Engineering. Cornell University.

Armero, F., Oller, S., 2000. A general framework for continuum damage models. II. Integration algorithms, with applications to numerical simulation of porous materials. Int. J. Solids Struct. 37, 7437–7463.

ASCE Task Committee on Finite Element Analysis of Reinforced Concrete Structures, 1982. Finite Element Analysis of Reinforced Concrete Structures. ASCE.

Borja, R., 1991. Cam-clay. Part II: Implicit integration of constitutive equations based on a nonlinear stress predictor. Comput. Meth. Appl. Mech. Eng. 88, 225–240.

Bresler, B., Scordelis, A.C., 1963. Shear strength of reinforced concrete beams. J. ACI (Jan), 51–72.

Crisfield, M.A., 1981. A fast incremental/iterative solution procedure that handles snap-through. Comput. Struct. 13, 55–62.

de Souza Neto, E.A., Perić, D., 1996. A computational framework for a class of fully coupled models for elastoplastic damage at finite strains with reference to the linearization aspects. Comput. Meth. Appl. Mech. Eng. 130, 179–193.

FEA-Ltd, 2002. Lusas User Manual. FEA Ltd, Kinston Upon Thames, UK.

Hassanzadeh, M., 1991. Behavior of fracture process zones in concrete influenced by simultaneously applied normal and shear displacements. Ph.D. Thesis, Lund Institute of Technology, Sweden.

Jefferson, A.D., 2003. Craft—a plastic-damage-contact model for concrete. I. Model description. International Journal of Solids and Structures, this issue.

Jefferson, A.D., Barr, B.I.G., 1995. Unified test procedure for evaluation the fracture characteristics of concrete. In: Wittmann, F.H., Zurich (Eds.), Proceedings of the Second International Conference on Fracture Mechanics of Concrete Structures.

Jirasek, M., Zimmermann, T., 1997, Nonlocal rotating crack model with transition to scalar damage. In: Owen, D.R.J., Onate, E., Hinton, E. (Eds.), Proceedings of the Fifth Conference on Computational Plasticity, Barcelona, Spain. pp. 1514–1521.

Johansson, M., Mahnken, R., Runesson, K., 1999. Efficient integration technique for generalized viscoplasticity coupled to damage. Int. J. Numer. Meth. Eng. 44, 1727–1747.

Larsson, R., Runesson, K., 1996. Implicit integration and consistent linearization for yield criteria of the Mohr–Coulomb type. Mech. Cohes. Frict. Mater. 1, 367–383.

Le Van, A., de Saxcé, G., 2000. Exact expressions for the plastic corrections and the consistent tangent modulus in rate-independent elastoplasticity. In: Proceedings of the European Congress on Computational Methods in Applied Science and Engineering, ECCOMAS 2000, Barcelona.

Lee, J., Fenves, G.L., 2001. A return-mapping algorithm for plastic-damage models: 3D and plane stress formulation. Int. J. Numer. Meth. Eng. 50, 487–506.

Mahnken, R., Tikhomirov, D., Stein, E., 2000. Implicit integration scheme and its consistent linearization for an elastoplastic-damage model with application to concrete. Comput. Struct. 75, 135–143.

Miehe, C., 1993. Computation of isotropic tensor functions. Commun. Numer. Meth. Eng. 9, 889–896.

Nooru-Mohamed, M.B., 1992. Mixed-mode fracture of concrete: an experimental approach. Ph.D. Thesis, Delft University of Technology, The Netherlands.

Ortiz, M., 1985. A constitutive theory for the inelastic behavior of concrete. Mech. Mater. 4, 67–93.

Ortiz, M., Martin, J.B., 1989. Symmetry-preserving return mapping algorithms and incrementally extremal paths: a unification of concepts. Int. J. Numer. Meth. Eng. 28, 1853–1939.

Ožbolt, J., Pivonka, P., Lackner, R., 2002, Three-dimensional FE analyses of fracture of concrete—material models and mesh sensitivity. In: Proceedings of the Fifth World Congress on Computational Mechanics, Vienna Austria.

Palazzo, V., Rosati, L., Valoroso, N., 2000. Computational issues of general isotropic elastic models. In: Proceedings of the European Congress on Computational Methods in Applied Science and Engineering, ECCOMAS 2000, Barcelona.

Petersson, P., 1981. Crack growth and development of failure zones in plain concrete and similar materials. Lund Institute of Technology, Sweden.

Rots, J.G., 1988, Computational modeling of concrete fracture. Ph.D. Thesis, Delft University of Technology, The Netherlands.

Rots, J.G., de Borst, R., 1987. Analysis of mixed-mode fracture in concrete. J. Eng. Mech. ASCE 113 (11), 1739–1758.

Simo, J.C., Hughes, T.J.R., 1998. Computational Inelasticity. Springer-Velag, New York.

Simo, J.C., Taylor, R.L., 1985. Consistent tangent operators for rate independent elasto-plasticity. Comput. Meth. Appl. Mech. Eng. 48, 101–118.

Tano, R., Klisinski, M., Olofsson, T., 1998. Stress locking in the inner softening band method: A study of the origin and how to reduce the effects. In: de Borst, R., Bicanic, N., Mang, H., Meschke, G. (Eds.), Proceedings of the EUROC-1998 Conference on Computational Modeling of Concrete Structures, Badgastein Austria. pp. 329–336.

Walraven, J.C., Reinhardt, H.W., 1981. Theory and experiments on the mechanical behavior of cracks in plain and reinforced concrete subjected to shear loading. Heron 26 (1A).